

Probing Terrace and Step Sites on Pt Nanoparticles Using CO and Ethylene

Matthew J. Lundwall, Sean M. McClure, and D. Wayne Goodman*

Department of Chemistry, Texas A & M University, College Station, Texas 77843

Received: December 17, 2009; Revised Manuscript Received: March 8, 2010

Temperature desorption spectroscopy (TDS) and infrared reflection absorption spectroscopy (IRAS) were used to study CO adsorption on the terrace and step sites of Pt nanoparticles grown in ultrahigh vacuum on SiO₂. The percentage of terrace sites obtained by TDS measurements from four average particle sizes (>4, 4.2, 3.3, 2.6, and 2.5 nm) are compared to a simple hard sphere counting model of a truncated cuboctahedron. It is demonstrated experimentally that when the average Pt particle size is reduced from 4.2 to 2.5 nm, the percentage of terrace sites decreases by ~50%, consistent with the hard sphere models. Pt particle morphology is further explored by blocking the terrace sites with ethylidyne (derived from ethylene). CO adsorption on the unoccupied sites of Pt nanoparticles precovered with ethylidyne demonstrates a continuous red-shift in IRAS with increasing particle size. Similarities and differences between Pt nanoparticles and high-index single crystals are discussed.

Introduction

The interaction of adsorbates with supported nanoparticles (NPs) is an important area of research from both a practical and fundamental perspective.^{1–5} Supported metal nanoparticles are commonly used in heterogeneous catalysis applications where the reactivity and selectivity are governed by the intrinsic properties of the nanoparticle (e.g., size, shape, electronic structure). Surface adsorbates have provided a means of assessing the electronic (ligand) and geometric (ensemble) variations at the surface,^{6–9} as these variations are often manifested in distinct changes in vibrational frequencies or desorption energies of adsorbates which can be analyzed with various spectroscopies.^{9–15} It is now well-known that undercoordinated surface atoms, (i.e., atoms having less than 9 nearest neighbors on FCC (111) metals) can have different chemical properties from fully coordinated surface atoms.¹⁶ These sites often play the defining role in the observed activity and selectivity of a catalyst.¹⁷ Thus, understanding the types of sites and characterizing their chemistry can help us clarify which reaction pathways are plausible on supported nanoparticles.

Van Hardeveld and Hartog (V&H)¹⁸ have demonstrated with statistical methods that particles <4 nm in diameter have the highest percentage of undercoordinated atoms. High index crystal planes (112, 335, 321, etc.) have therefore been of central importance for fundamental studies as these surfaces offer a high density of defects (steps, kinks, and corner atoms),¹⁶ structural features which represent the largest percentage of available sites on dispersed metal catalysts. Insights gained from stepped metallic surfaces are numerous; however, these systems do not accurately model the electronic/size or substrate effects that may influence adsorption on dispersed-particle catalysts, the so-called “material-gap”.^{19–21} Moreover, high surface area catalysts can limit fundamental investigations because measurements can be influenced by diffusion limitations or by metal precursor contaminants from preparation (e.g., chlorine). Our group^{13,17,19,20,22–24} and others^{21,25–28} have been motivated by these issues and have proposed and implemented the preparation of

model oxide-supported dispersed metal NPs in ultrahigh vacuum (UHV). These surfaces have a well-defined size distribution, offer sizes between ~1 – 10 nm, and are not complicated by contaminants associated with solution based preparations.

Two of the most well studied adsorbates to date are CO and C₂H₄. Much work has been performed on the adsorption of CO and coadsorption of CO and ethylene on the surface of low-index single crystals.^{13,29–36} These studies have provided information on surface structure, charge transfer, and interactions between adsorbates. To a much lesser extent, such interactions have been studied on supported catalysts and high-index surfaces.^{14,37–39} Here, we demonstrate the influence of Pt particle size on the adsorption of CO and the coadsorption of ethylidyne (derived from ethylene) and CO. We extend this analysis to directly probe the percentage of highly coordinated and undercoordinated atoms on the surface of Pt NPs. The results obtained from our adsorption measurements are compared to statistical estimates of surface sites based on simple geometrical models and arguments. To our knowledge, this is the first effort to quantify the percentage of step and terrace sites simultaneously on the surface of Pt NPs as a function of Pt NP size using probe molecules in UHV. Pt in this sense allows for separation of step and terrace features in the CO adsorption/desorption spectra due to the strong variation in electronic structure at the step.^{40,41}

Experimental Section

Experiments were performed in a UHV surface analysis chamber described elsewhere.⁴² Briefly, this apparatus consists of a surface preparation analysis chamber equipped with Auger electron spectroscopy (AES), thermal desorption spectroscopy (TDS), and vapor deposition capabilities, coupled with a contiguous IR cell equipped with CaF₂ windows for infrared reflection absorption spectroscopy (IRAS) measurements. Sample heating was carried out resistively and monitored by a C-type W/Re thermocouple spot-welded to the sample.

Pt/SiO₂ samples were prepared on a Mo(112) single crystal substrate ($d = 0.986$ cm). Prior to SiO₂ film preparation, the Mo(112) was cleaned via Ar⁺ sputtering and annealing cycles, as verified via AES. SiO₂ films were grown by Si vapor deposition in a 1×10^{-6} Torr O₂ ambient at $T = 650$ K,

* To whom correspondence should be addressed. Telephone: +1 979 845 0214. Fax: +1 979 845 6822. E-mail: goodman@mail.chem.tamu.edu.

followed by annealing at 1000 K in 2×10^{-5} Torr O_2 . The SiO_2 film thickness is estimated to be ~ 1.5 nm, based on the near complete attenuation of the Mo(187 eV) signal.^{43,44} Next, Pt was vapor deposited on the SiO_2 film at $T = 300$ K to the desired coverage. The Pt deposition rate (Pt $\sim 0.1 - 0.2$ ML/min) and total coverage were determined from an AES break-point measurement on the Mo(112) substrate; the total surface area was further validated by CO chemisorption. Pt particle size and distribution measurements were conducted in a separate scanning tunneling microscopy (STM) chamber, the results of which have been discussed in a previous publication.²³ Average particle diameters $\langle d_p \rangle$ and standard deviations σ were determined as follows: 2.5 nm, $\sigma = 0.5$ nm (0.5 ML Pt); 2.6 nm, $\sigma = 0.5$ nm (1 ML); 3.3 nm, $\sigma = 1$ nm (2 ML); 4.2 nm, $\sigma = 1$ nm (4 ML).

Ultrahigh purity (UHP) ^{12}CO was utilized for all IRAS and TDS experiments; CO gas was further purified by passing over a heated 3 Å molecular sieve, followed by a LN_2 trap. UHP ^{13}CO ($m/z = 29$) (99%) was also used in several experiments, primarily to provide clarity in CO-TDS spectra obtained from ethylene ($m/z = 28$) pre-exposed surfaces. UHP C_2H_4 (99.98%) utilized for TDS and IRAS experiments was further purified by multiple freeze-pump-thaw cycles. Gases were delivered to the surface through conventional leak valves (1 L = 1×10^{-6} Torr s). Pt/ SiO_2 surfaces were cleaned in a 1×10^{-6} Torr O_2 ambient at $T = 600$ K for 10 min to remove residual carbon (from the Pt vapor deposition process) prior to CO-IRAS and CO-TDS measurements.

CO-IRAS measurements were conducted with a Mattson Cygnus 100 infrared spectrometer. IR spectra were collected using 512 scans at a resolution of 4 cm^{-1} . Background spectra were obtained on the clean Pt/ SiO_2 /Mo(112) surfaces in UHV for the IRAS measurements. CO-TDS measurements were obtained using a UTI Instruments quadrupole mass analyzer and a sample heating rate of 5 K/s. Background spectra were also obtained on the SiO_2 /Mo(112) surface prior to Pt deposition for all TDS and IRAS spectra. As expected, TDS spectra demonstrated negligible CO uptake from the sample leads (desorbed < 100 K), indicating CO adsorption and desorption is occurring on the Pt particles. IRAS spectra did not show any CO adsorption on SiO_2 /Mo(112). CO adsorption on Pt/ SiO_2 /Mo(112) from residual CO in the UHV ($P_{\text{base}} = 5 \times 10^{-10}$ Torr) background was also negligible. As will be discussed, the two desorption features observed in the CO-TDS spectra were separated using a simple Gaussian fit followed by integration to assess the relative percentage of terrace and step sites on the Pt/ SiO_2 surfaces as a function of particle size. This kind of analysis has been applied successfully by previous investigators in studies of stepped Pt single crystal surfaces.⁴⁵

Results

Figure 1 displays three IRAS spectra each obtained at 300 K in a $P = 1 \times 10^{-7}$ Torr CO ambient on 2.6 nm Pt particles. As discussed in the Experimental Section, Pt/ SiO_2 surfaces are prepared and then cleaned in O_2 at 600 K to remove residual carbon. Spectrum (a) depicts cooling the surface in 1×10^{-7} Torr CO from 500 to 300 K after O_2 cleaning and represents a saturated CO surface at 300 K. Two features are present, one at 2077 cm^{-1} and another at 2094 cm^{-1} . As will be discussed shortly, these correspond to *steplike* and *terrancelike* adsorption sites on the Pt NP surface, respectively. The sample is then heated to the indicated temperatures of $T = 500$ K (b) and $T = 600$ K (c) in the above CO environment followed by cooling to 300 K in CO. All three spectra (a–c) show approximately the

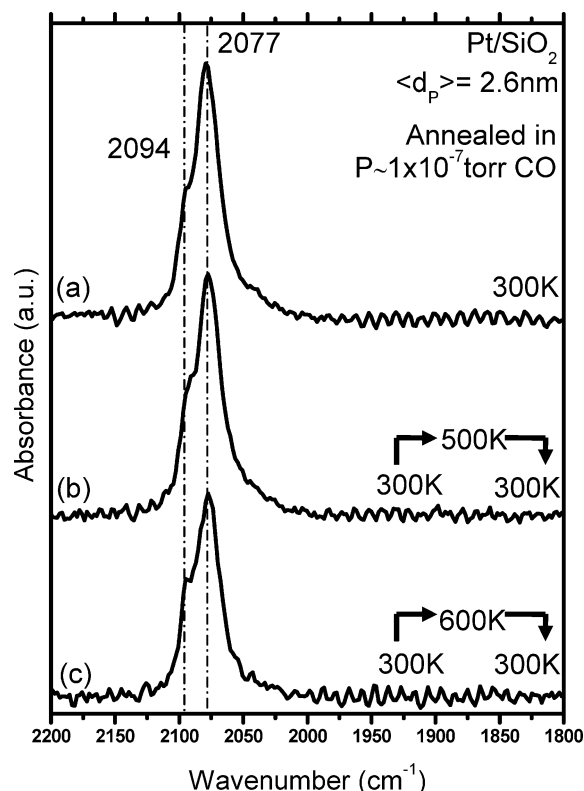


Figure 1. CO-IRAS of $\langle d_p \rangle = 2.6$ nm Pt nanoparticles on SiO_2 . All spectra were acquired consecutively at $T = 300$ K in a background of $P = 1 \times 10^{-7}$ Torr CO. Spectrum (a) cooled from $T = 500$ to 300 K in CO, (b) annealed to $T = 500$ K in CO followed by cooling to 300 K in CO, and (c) annealed to $T = 600$ K followed by cooling to 300 K in CO.

same adsorption features and intensities, indicating CO adsorption is reversible for both features under all three conditions. Additionally, these data illustrate that Pt/ SiO_2 surfaces are essentially free of surface oxygen from the cleaning procedure, as indicated by the lack of CO stretching associated with Pt-oxide surfaces;⁴⁶ in other words, CO is adsorbed on metallic Pt NPs. Further analysis of the 2.6 nm particles is presented in the temperature dependent CO-IRAS data of Figure 2. A CO saturated surface labeled $\theta_{CO} = 1$ was prepared by cooling from $T = 500$ to $T = 300$ K in $P = 1 \times 10^{-7}$ Torr CO as in Figure 1a followed by complete evacuation to achieve UHV conditions ($P < 10^{-9}$ Torr). From here, the IRAS spectrum was sequentially acquired at the indicated temperatures of Figure 2. The feature at 2094 cm^{-1} red-shifts 9 cm^{-1} to 2085 cm^{-1} at a temperature of $T = 320$ K and then disappears at a temperature of $T = 375$ K where only a single feature can be observed at 2060 cm^{-1} . Further heating leads to a shift to 2046 cm^{-1} at 425 K followed by complete desorption at $T = 450$ K.

Figure 3a shows NP size dependent (2.5 to >4 nm) CO-IRAS spectra each acquired at 150 K. Each surface was cooled from $T = 500$ to 150 K in $P = 1 \times 10^{-7}$ Torr CO followed by IRAS spectral acquisition in a $P = 1 \times 10^{-7}$ Torr CO environment; all features in Figure 3a represent CO saturated surfaces. For clarity, the 2.5, 2.6, and 3.3 nm IRAS data have been multiplied by a factor of 10, 4, and 3, respectively. Two features are clearly visible at all particle sizes and qualitatively correspond to terrancelike (high-wavenumber) and steplike (low-wavenumber) adsorption. Upon increasing particle size, the terrancelike feature of the 3.3 nm particles increases in intensity and becomes approximately equal to the steplike feature. The terrancelike feature further increases and becomes the dominant feature for

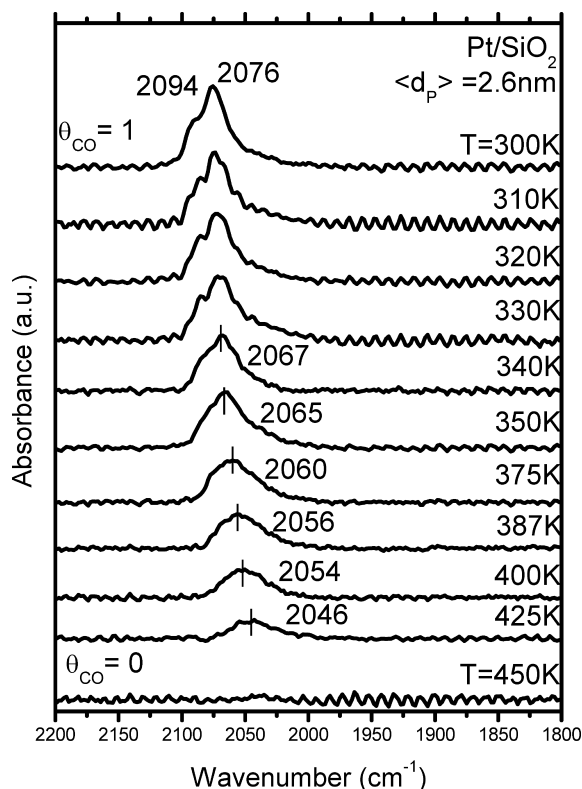


Figure 2. Temperature dependent CO-IRAS of $\langle d_p \rangle = 2.6$ nm Pt nanoparticles on SiO₂. The sample was first cooled from $T = 500$ to 300 K in 1×10^{-7} Torr CO as in Figure 1a followed by evacuation to UHV and heating to the indicated temperatures. $\theta_{\text{CO}} = 1$ represents a maximum coverage of CO at $T = 300$ K in UHV.

particles > 3.3 nm. A third feature on > 4 nm NPs at 1850 cm^{-1} can also be observed (not shown). All three features qualitatively correlate to what has been observed on highly stepped Pt single crystals with particular emphasis to the Pt(112) and Pt(335) crystal planes^{9,47–53} (discussed below) and can be qualitatively attributed to terracelike and steplike adsorption.

The two distinct CO stretching features observed in CO-IRAS can be further explored with TDS as shown in Figure 3b. Figure 3b displays a saturation dose of ^{13}CO on 2.5 nm to > 4 nm NPs where two features develop with increasing NP size. On small NPs, the first feature to develop is a high temperature one at 450 K followed by a low temperature feature at 350 K as the NP size increases. The feature at 450 K grows for increasing NP size and becomes saturated while the feature at 350 K continuously grows with an increase in NP size. A similar two-peak desorption profile was observed in thermal desorption spectra of CO from Pt(335)^{9,47} and Pt(112).^{9,52,53} The high-temperature feature can therefore be qualitatively assigned to steplike adsorption, and the low-temperature feature to terracelike adsorption (to be discussed). The profile of each spectrum in Figure 3b was Gaussian fit and separated into terracelike and steplike profiles (inset Figure 3b). The area of the terracelike feature for each particle size was normalized to the combined integrated area of its respective steplike and terracelike features and plotted as % CO-TDS terrace sites (to be discussed below) with respect to NP size in Figure 7.

Freshly prepared NP surfaces were each exposed to a 20 L dose of ethylene at 300 K followed by cooling the surfaces in $P = 1 \times 10^{-7}$ Torr CO from $T = 300$ to 150 K. IRAS spectra were subsequently run on these Pt NPs and are presented in Figure 4a where only the CO stretching region has been displayed. The step and terrace double-feature observed on the

clean NPs in Figure 3a is absent from the NP spectra of Figure 4a and present only as a single-feature. This feature is red-shifted for NPs > 2.5 nm with respect to both terrace and step features on the clean NPs. Moreover, Figure 4a displays a red-shift that is dependent on size which can be more clearly seen in Figure 4b. Both the clean and ethylene exposed NPs do, however, display a similar feature at 1850 cm^{-1} on NPs > 4 nm.

For TDS, each clean NP surface was exposed to 20 L of ethylene at 300 K followed by cooling in 1×10^{-7} Torr ^{13}CO to 150 K followed by evacuation. ^{13}CO -TDS spectra from the ethylene pre-exposed NPs of 2.5 and 4.2 nm are plotted against their clean NP profiles (from Figure 3b) in Figure 5. The desorption features can be correlated to the CO desorption features observed from the clean NPs (discussed later); these features are referred to as terracelike and steplike, respectively. For > 4.0 nm NPs (and all > 2.5 nm NPs discussed later), each peak is attenuated when compared to their respective clean surfaces. The steplike feature on ethylene exposed 4.2 nm NPs has approximately the same intensity as the terrace feature. The leading edge of the desorption profile on ethylene pre-exposed surfaces matches that of the clean surface for all NP sizes. There is almost no change between the clean and ethylene exposed 2.5 nm TDS profile in Figure 5a.

Discussion

CO Adsorption. Pt NPs are known to grow spherical on SiO₂ and exhibit cuboctahedral structures with (111) and (100) type facets.^{18,54–57} Adsorption measurements presented in this paper indicate two desorption features in the CO-TDS profiles from Pt NPs, of which a low temperature desorption feature is dominant on particles > 3 nm. CO-TDS measurements on Pt(100)^{53,58} and Pt(111)⁵³ low-index crystal planes exhibit desorption profiles that are very different from Pt NPs as both crystals each reveal only one CO desorption feature. CO desorption from Pt(110)^{31,53} reveals two features with the low-temperature feature less intense than the high-temperature feature. Kinked surfaces such as Pt(321)¹² also do not have comparable CO desorption spectra to Pt NPs and will not be addressed at present. Only single crystals with a combination of (111) and (100) planes in correct proportions (discussed below) can provide a reliable means of indirectly assessing the structure of Pt nanoparticles grown on SiO₂ in UHV.

Plotted in Figure 6 is the percentage of terrace features on the surface of numerous stepped crystal planes. In this figure, truncated cross sections for both Pt(335) and Pt(112) are presented in step–terrace notation.⁵⁹ Following the designation by V&H,¹⁸ the C_9^3 terrace sites are described as being 9-fold coordinated and exist in the (111) plane while the C_{10} terrace sites have an additional atom, lie below the step edge, and are part of both the (111) and (100) crystal planes. The ratio of terrace sites to total surface sites for this model is plotted against the terrace width in Figure 6. It can be seen that as the width of the terrace increases, the total percentage of highly coordinated C_9^3 and C_{10} sites increases. Also presented in Figure 6 are the approximate total $\text{C}_9^3 + \text{C}_4^{5,8}$ terracelike sites that can exist on Pt NPs of different diameters; $\text{C}_4^{5,8}$ atoms have the highest coordination on a (100) surface. For this plot, a simple hard sphere counting model was used where NPs are described as truncated cuboctahedron “caps”, have a Pt atomic diameter of $d_{\text{Pt}} = 0.28$ nm, and are truncated at a height equal to $\sim 1/2$ the diameter (see Figure 6). From the plot in Figure 6, it can be seen that particles > 4 nm exhibit a percentage of terracelike sites ($\text{C}_9^3, \text{C}_4^{5,8}$) that are in accordance with the (112) and (335) crystal planes (i.e., the local structure surrounding the (112) and

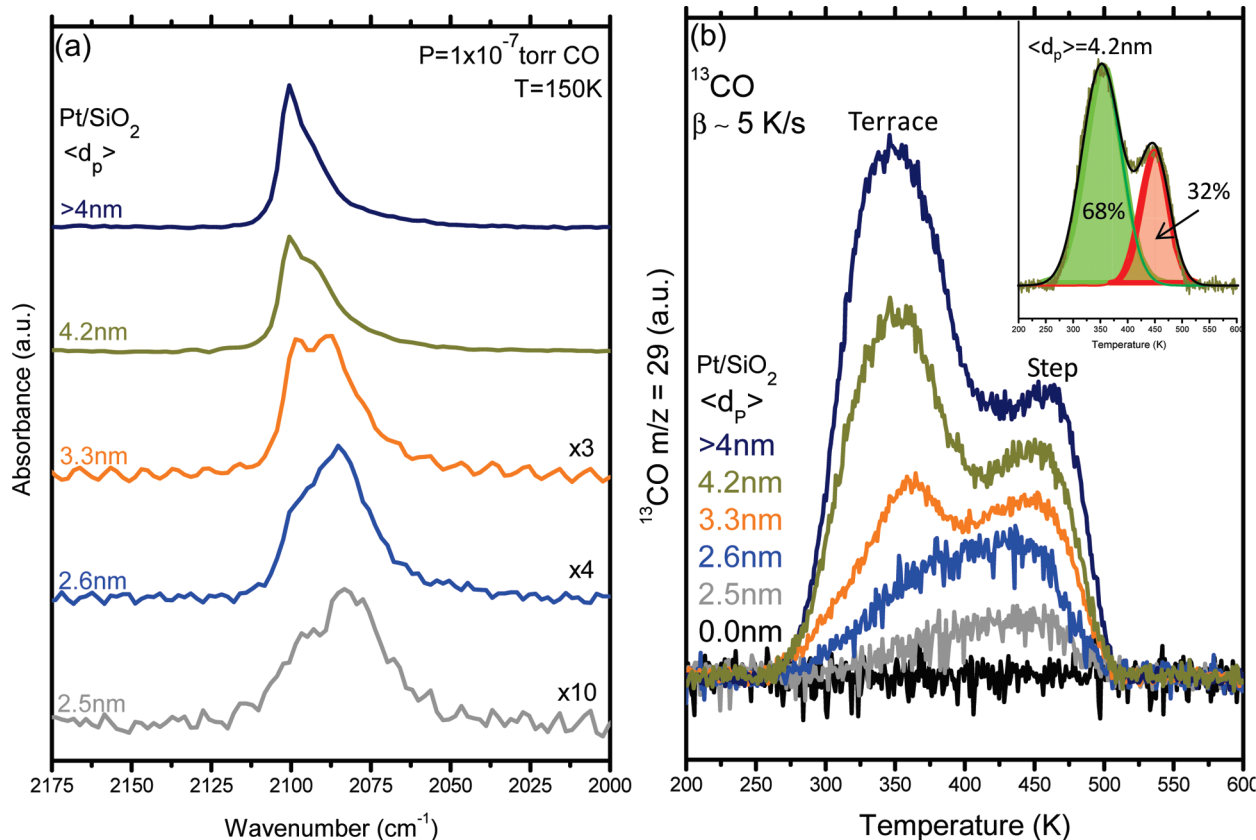


Figure 3. (a) CO-IRAS spectra of Pt nanoparticles of varied size on SiO₂ acquired at $T = 150$ K. Each surface was cooled from $T = 500$ to 150 K in 1×10^{-7} Torr CO and each acquired in a background of 1×10^{-7} Torr CO. For clarity, spectra $\langle d_p \rangle = 2.5$, 2.6 , and 3.3 nm have been multiplied by a factor of 10, 4, and 3, respectively. These data are also presented in Figure 4b for clarity. (b) CO-TDS spectra of Pt nanoparticles of varied size on SiO₂. Each surface was cooled from $T = 500$ to 90 K in $P = 1 \times 10^{-7}$ Torr in ^{13}CO followed by evacuation. Each desorption profile has a heating rate of 5 K/s. The inset is an example of the Gaussian fit and deconvolution used to calculate the percentage of terrace sites plotted in Figure 7.

(335) planes closely resembles that of nanoparticles). Terrace width effects for CO TDS on Pt(112) and Pt(335) have not been observed.^{9,60} In fact, CO desorption profiles on the (112) and (335) crystal planes *resemble* that of dispersed Pt catalysts.⁹ An ideal unreconstructed (113)⁶¹ crystal plane in this model has a qualitative particle size limit of 3 nm. As particles drop below <3 nm, the percentage of terracelike features, C_9 and C_8 , drops below 50% of the total surface area. As particle size continues to decrease, the terracelike features asymptotically approach 0% . For this reason, it is essential to perform direct measurements on small Pt particles since geometric arguments have no single crystal analogue for particles < 3 nm. Indeed, we see similar desorption profiles and peak temperatures in our TDS as in the Pt(533) for particle sizes > 2.5 nm. Pt(533) exhibits an intense low-temperature CO-desorption terrace feature from a fully saturated surface.⁹ The terrace feature on the Pt(112) is less pronounced than on the Pt(335) as a result of the smaller terrace.⁹ Therefore, from geometrical arguments and CO desorption profiles,⁹ it can be inferred that larger particles (i.e., 4.2 nm) should exhibit a more pronounced terrace feature as in the desorption profile of Pt(533) while smaller particles (i.e., 3.3 nm) should exhibit a reduced terrace feature as in Pt(112). This behavior is exactly what is observed when comparing the percentage based on our ^{13}CO -TDS spectra with the percentage based on calculated particle sizes (see Figure 7). As an important note, $C^{4,5}_8$ sites on Pt NPs may interact differently with CO than C^3_9 sites but this cannot be distinguished in CO TDS or IRAS spectra.

When the NP drops to 2.5 nm, the terrace feature in the TDS becomes almost completely attenuated and step features become

dominant (Figure 3b). The trend in TDS measurements indicates that the average ΔH_{ads} is enhanced on small Pt NPs. Indeed, experimental data for approximated ΔH_{ads} are shown to increase with decreasing size.^{27,62} The result is caused by the increased density of step sites on the surfaces of smaller Pt particles, sites which bind CO more strongly than terrace sites. The step sites on larger particles (e.g., >4 nm) compose $<30\%$ of the surface area and thus do not have a large contribution to the overall ΔH_{ads} value. The enhancement in ΔH_{ads} for small particles has also been shown to increase the activation energy for the CO oxidation reaction on small Pt particles (1.7 nm) on Pt/Al₂O₃ model catalyst surfaces.⁶² An increase in ΔH_{ads} is also observed experimentally when comparing stepped Pt(210) to planar Pt(111), ~ 142 kJ/mol and ~ 109 kJ/mol, respectively.⁵³ From these data, it does not appear that the overall Pt NP size greatly affects the adsorption energy at a step, as indicated by an almost constant peak desorption temperature for a step site (Figure 3b) for various Pt particle sizes. This would indicate that the increased ΔH_{ads} observed on small Pt NPs is not a unique aspect of Pt NPs alone and that it is simply a continuation of the intrinsic property observed on high index Pt single crystals.

At this point, it is worth noting the similarities between our Pt/SiO₂ system and Pt NPs on other supports (i.e., Al₂O₃) and also with model and high surface area technical catalysts. Zafiridis et al.⁶² were able to probe Pt/Al₂O₃ prepared in UHV and observed one CO desorption feature for an average particle size of 1.7 nm and two CO desorption features for a particle size of 14 nm consistent with step and terrace binding. Greenler et al. indicate $\nu(\text{CO}) = 2063$ cm⁻¹ on a step for an average size range of $d_p = 4$ nm,⁶³ similar to a step (2065 cm⁻¹) on Pt(335).⁴⁷ Our

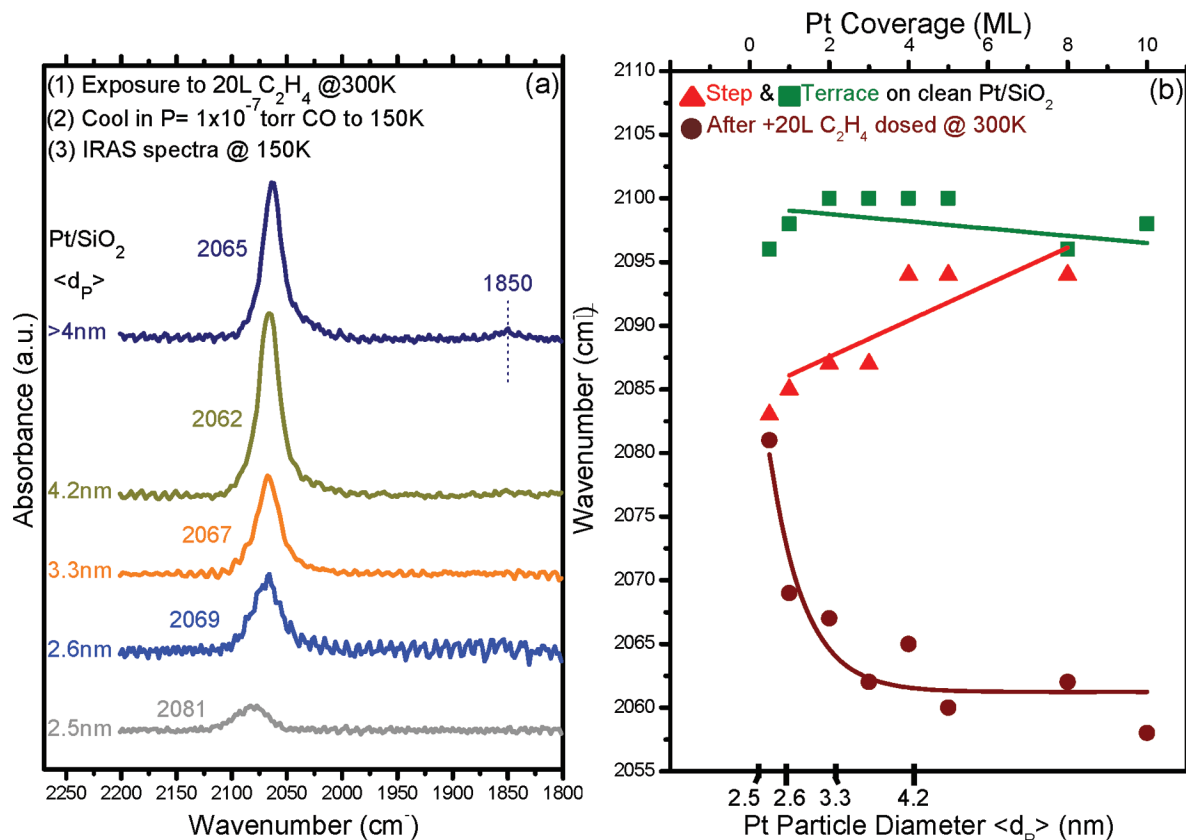


Figure 4. (a) CO-IRAS spectra of Pt nanoparticles of varied size on ethylene pre-exposed surfaces. Each Pt/SiO₂ surface was exposed to 20 L of ethylene at $T = 300$ K to form ethylidyne ($\text{Pt}_3\equiv\text{C}-\text{CH}_3$) followed by evacuation and then cooled from $T = 300$ to 150 K in $P = 1 \times 10^{-7}$ Torr CO. All spectra were acquired at 150 K in a background of $P = 1 \times 10^{-7}$ Torr CO. These data are also plotted in figure 6 for clarity. (b) CO-IRAS wavenumber versus Pt nanoparticle size for clean and 20 L ethylene pre-exposed Pt/SiO₂ surfaces. Data points are acquired from Figures 3a and 4a. Particle size estimates are based on previous data obtained using STM.²³

results in Figure 2 show that a step site with a vibrational feature at 2060 cm^{-1} for a particle size of 2.6 nm correlates well with these studies and that of other high surface area Pt/Al₂O₃ samples (2060 cm^{-1} ; ref 64). Similar IR results on technical Pt/SiO₂ catalysts with a size range of 5–15 nm display an absorption near 2050 cm^{-1} using transmission IR⁶⁵ which has also been observed on a commercial Pt/Al₂O₃ catalyst.⁶⁶

An excellent treatment concerning the effect of Pt-atom coordination on $\nu(\text{CO})$ is demonstrated by the calculations of Brandt and Greenler et al.⁶⁷ Data from the low coverage limit of CO on high-index crystals were used to assess singleton stretching frequencies of CO for a number of Pt surface coordination numbers assuming an “idealized” condition. It was determined that a linear correlation exists between Pt coordination and $\nu(\text{CO})$, consistent with reports of this effect from experimental data in the literature.⁶⁸ In a second paper, the same authors were able to extend this analysis to Pt nanoparticles of cuboctahedral geometry and to show a correlation in $\nu(\text{CO})$ and IR intensity between theory and experiment.⁶⁹ Calculations demonstrated dipole coupling shifts can depend on the in-phase and out-of-phase stretching modes of CO adsorbed on different regions and also on the concentration of CO in the adlayer.⁶⁹ It then becomes obvious that assignment of $\nu(\text{CO})$ from experimental data to a specific coordination number on a NP is a difficult task because of the various factors which can potentially influence changes in $\nu(\text{CO})$. For example, a $\Delta\nu(\text{CO})$ can also be demonstrated for the 2.6 nm NPs by increasing the temperature from $T = 300$ to 340 K, $\Delta\nu(\text{CO}^{\text{terrace}}) = 9\text{ cm}^{-1}$, or from $T = 350$ to 425 K, $\Delta\nu(\text{CO}^{\text{step}}) = 19\text{ cm}^{-1}$, as in Figure 2. Increasing the temperature leads to an decrease in the CO

adlayer as observed by TDS, and therefore, $\Delta\nu(\text{CO}^{\text{terrace}}) = 9$ or $\Delta\nu(\text{CO}^{\text{step}}) = 19\text{ cm}^{-1}$ can be related to the dipole–dipole induced shift known to occur for CO adsorption on Pt.^{70,71} Figure 7 demonstrates that 60% of the surface area of 2.6 nm Pt NPs are consumed by step sites (e.g., C₇, C₆). It can be concluded that the remaining 40% of the surface has CO molecules bound to higher coordination sites (e.g., C₉, C_{4,5,8}). Coupling between step sites of different coordination, step sites of identical coordination, step–terrace coupling, and terrace–terrace coupling are all known to affect $\nu(\text{CO})$.⁶⁹ Therefore, experimental data concerning the magnitude of $\Delta\nu(\text{CO})$ based on particle size and Pt-atom coordination at the surface is questionable.^{37,68} Based on the results of Figure 2, the only estimate we can make with confidence with regard to $\nu(\text{CO})$ and its relation to Pt-atom coordination is that the singleton $\nu(\text{CO})$ on a step site must be below 2060 cm^{-1} in the size range of 2.5 nm. This is consistent with the calculations of Brandt et al.^{67,69}

For our IRAS data in Figure 3a, with increasing average particle size, the intensity of the terracelike feature gains intensity while the steplike feature also gains intensity. This effect is not observed on stepped single crystals. On these crystals, the intensity of terrace CO species is enhanced at the expense of step CO intensity through dipole interactions.^{11,70} This effect requires close proximity (r^{-3} dependence¹⁰) of the CO molecules in the adlayer and can be inferred that, in the absence of intensity sharing, CO must be on distinctly different particles; that is, the overall intensity from step-only absorption in Figure 3a is a combination of all particles in the size distribution. This emphasizes another limitation for direct comparisons between stepped single crystals and high surface

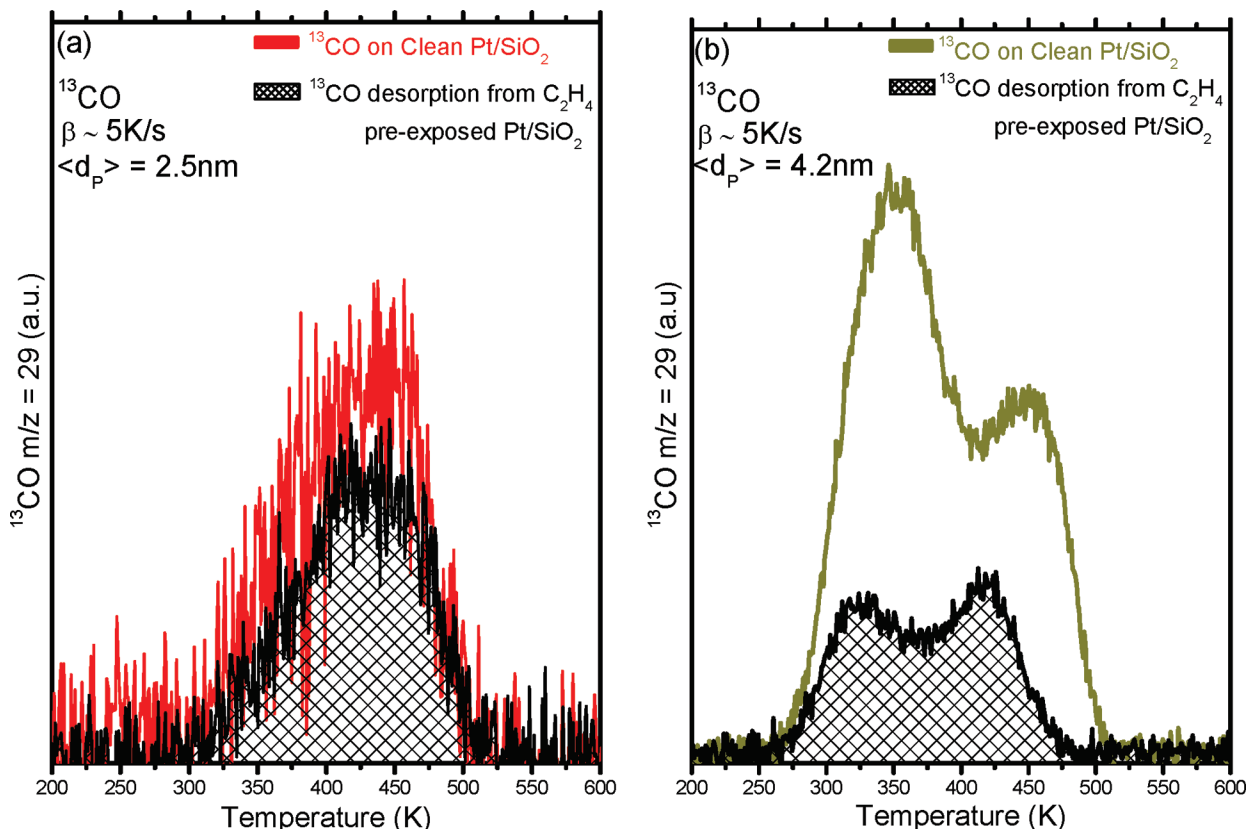


Figure 5. (a,b) ^{13}CO -TDS spectra from clean (obtained from Figure 3b) and ethylidyne-covered nanoparticles of $\langle d_p \rangle = 2.5$ and 4.2 nm. Each Pt/SiO₂ surface was exposed to 20 L of ethylene at 300 K to form ethylidyne ($\text{Pt}_3\equiv\text{C}-\text{CH}_3$), followed by evacuation and then cooling from 300 to 90 K in $P = 1 \times 10^{-7}$ Torr in ^{13}CO . Each desorption profile has a heating rate of 5K/s. The area under each ethylidyne-covered surface profile has been shaded for clarity.

area catalysts⁶⁶ (i.e., both model and technical particle systems can exhibit *similar* spectra to single crystals, although intensities and frequencies can be quite different). Other adsorption geometries such as bridging Pt_2CO at 1850 cm^{-1} that have been reported on Pt(112) and Pt(335)⁹ single crystals are also observed on our >3.3 nm NPs (not shown). The nature of this species cannot be determined with confidence, since terrace and step bridging CO are known to exist on both Pt(112) and Pt(335). CO bridging on the (100) crystal planes is also known to exhibit an absorption frequency in this region.⁷²

CO and Ethylene Adsorption. It is well established that three prominent ethylene derived species can exist on Pt (i) π -bonded ethylene ($\text{Pt}-\text{C}_2\text{H}_4$), (ii) di- σ -bonded ethylene ($\text{Pt}-\text{CH}_2\text{CH}_2-\text{Pt}$), (iii) ethylidyne ($\text{Pt}_3\equiv\text{C}-\text{CH}_3$).^{28,32-35,37,39,71-76} In a UHV environment, the π and di- σ species are only formed at temperatures $T < 250$ K. The ethylidyne species forms at $T > 250$ K and can only be manifested on (111) crystalline terraces.^{33,76} Measurements by a number of researchers on both Pt and other transition metals indicate ethylidyne to be the dominant species on the surface at $T \sim 300$ K.^{13,28,32,33,36,38,73-76} On our Pt particles, we observed the ethylidyne methyl symmetric mode $\delta_s(\text{CH}_3)$ at ~ 1340 cm^{-1} with IRAS on NPs > 3.3 nm at 300 K (not shown), in good agreement with literature values. Based on literature data which indicate CO adsorption can displace both the di- σ -bonded and π -bonded ethylene,³⁹ we propose ethylidyne to be the only species on the surface. Our results in Figures 4 and 5a show CO to be uninhibited on NPs of 2.5 nm, indicating 2.5 nm NPs do not have the ensemble required to support ethylidyne under the present conditions. As the average particle size and terracelike sites increase, the total surface concentration of ethylidyne also increases (Figure 7,

discussed below). A continuous red-shift in $\nu(\text{CO})$ follows this trend that is opposite the effect of CO dipole-dipole coupling interactions which is known to blue-shift with increasing CO coverage on Pt-group metals.^{70,71} From our data, it is not clear which interaction, Stark or charge transfer, between ethylidyne and CO is dominant.¹³ Some insight can be gained from the results of Figure 5b which indicate two CO desorption features from the ethylidyne covered surface. For this, three facts are invoked from the literature: (i) ethylidyne requires an FCC (111) ensemble,^{32,33,73-76} (ii) ethylidyne is stable between ~ 300 and 400 K,^{36,73} and (iii) ethylidyne has a surface coverage of $\theta \sim 0.25$ on Pt(111) because of repulsive interactions between ethylidyne.^{33,76} From these three facts, three arguments can be made concerning the nature of the two CO desorption features in Figure 5b. First, the concentration of ethylidyne on the NPs must be limited due to repulsive interactions. Second, similarly with Pt(111) and Pd(111), the unoccupied terrace sites are still available for CO adsorption.^{36,38} Third, step sites on NPs are also available for CO adsorption. As an example, the terrace feature from CO-TDS of the ethylidyne-covered NPs for various particle sizes is plotted along with CO-TDS from the terrace feature of clean NPs in Figure 7. Here, ethylidyne is shown to occupy $\sim 18\%$ of total sites on a surface containing 4.2 nm NPs. This is less than the $\sim 68\%$ of terracelike sites [(100) + (111)] shown to exist on clean 4.2 nm NPs (Figure 7) and indicates $\sim 50\%$ of terrace sites are still available for CO adsorption. Based on these data, it can be inferred that both step and terrace CO are present on the ethylidyne-covered NPs and desorb as two separate features in ^{13}CO -TDS (Figure 5b). Since only one CO-IRAS feature is observed, it can also be inferred that both step and terrace CO experience a similar local environment on

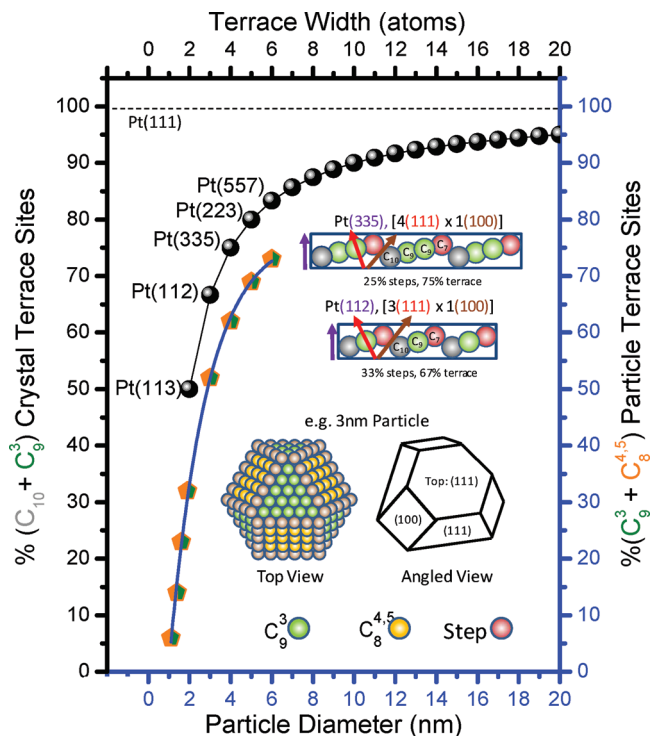


Figure 6. Percentage of highly coordinated terrace sites ($C_9^3 + C_{10}$) on various stepped Pt single crystals plotted against the total terrace width. Insets are the truncated cross sections of Pt(335) and Pt(112) and indicate the (111) and (100) crystal orientations. Also plotted are the highly coordinated ($C_9^3 + C_{4.5}^8$) sites that are present on Pt nanoparticles of varied size. Nanoparticle statistics are obtained from a simple hard sphere counting model assuming Pt particles grow in the (111) orientation and can be described as truncated cuboctahedron “caps”. An example of a 3 nm particle is presented in the figure.

ethylidyne-covered NPs. As can be seen from the data of Figure 4a, $\nu(\text{CO})$ is relatively sharp and symmetrical for each particle size, indicating the homogeneity of the adsorption sites. The effect of atomic hydrogen from ethylene decomposition on $\nu(\text{CO})$ IR frequency on high-index Pt single crystals shows a repulsive behavior and the formation of compressed one-dimensional CO islands on the surface.^{45,77} The hydrogen concentration is small considering the percentage of dissociated ethylene and the concentration of step sites and therefore should not have an appreciable effect on the CO stretching frequency. Possibly, charge transfer to the CO $2\pi^*$ antibonding orbital⁷⁸ becomes enhanced at a terrace site which shifts its absorption toward that of CO bound to step site. Dipole coupling between step and terrace CO gives rise to an intense symmetrical feature. Au clusters are also shown to have an effect where two CO desorption features can be present in CO-TDS but show only one IR absorption.¹⁵ Interestingly, a feature at 1850 cm^{-1} which can be related to a bridging CO species ($\text{Pt}_3\text{-CO}$ or $\text{Pt}_2\text{-CO}$) is present on $>3.3\text{ nm}$ NPs and is unaffected by the presence of ethylidyne. Possibly, this species may also exist for smaller Pt particles, but the concentration may be below the detection limit of our current IRAS setup. On Pt(112), bridging CO forms for high CO concentrations on both terrace and step atoms. It would appear that the sites occupied by $\nu(\text{CO}) = 1850\text{ cm}^{-1}$ on a Pt particles are not active in the formation of ethylidyne as would be expected based on the results from stepped crystal planes.

In Figure 7, we make a quantitative estimate of the amount of surface covered with ethylidyne by performing ^{13}CO -TDS on the Pt NPs before and after exposure to ethylene at 300 K. Figure 7 shows the percent terrace from both the terrace sites

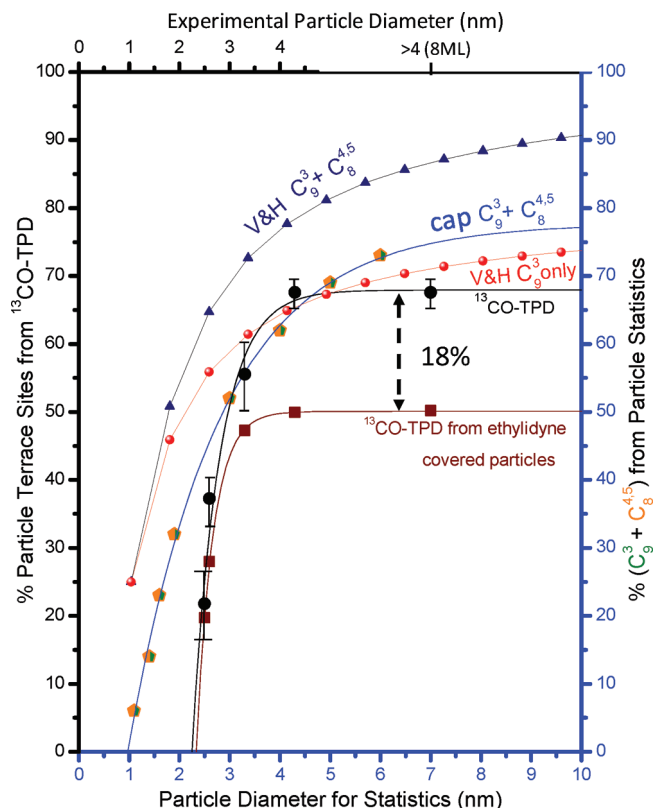


Figure 7. Percentage of terrace sites obtained experimentally from ^{13}CO -TDS on clean and ethylidyne-covered Pt nanoparticles. Also plotted is the percentage of terracelike C_9^3 and $C_{4.5}^8$ sites from Figure 6 along with statistics from V&H.¹⁸ Particle size estimates are based on previous data obtained using STM.²³ Error bars are obtained from the standard deviation ($\pm\sigma$) of repeated measurements.

obtained from the TDS profiles of Figure 3b and the percentage of available terrace sites after exposure to ethylene in Figure 5. For reference, we utilize a calculation for a truncated cuboctahedron cap of $\sim 4\text{ nm}$ which has a surface area of consisting of 237 atoms of which 93 atoms have (111) C_9^3 coordination. Based on Pt(111) which exhibits an ethylidyne ($\text{Pt}_3\text{C}\equiv\text{CH}_3$) saturation of $\sim 25\%$,³³ our 4 nm model particle can accommodate ~ 8 ethylidyne species. Experimental results in Figure 7 demonstrate ethylidyne to block approximately 18% of a surface covered with 4 nm particles. Our Pt/SiO₂ samples with particle sizes in the range of $\sim 4\text{ nm}$ (4 ML Pt) are shown to exhibit 8.1×10^{14} total surface sites/cm² based on our previous studies²³ of which $\sim 68\%$ are terrace (Figure 7). Knowing our approximated surface density of particles $\sim 8.9 \times 10^{12}$ per cm² and assuming a narrow size distribution, we can estimate the number of ethylidyne per 4 nm NPs to be ~ 4 ethylidyne molecules. This is in fair agreement with the ~ 8 ethylidyne molecules estimated from a 4 nm model-particle calculation. As the average particles size decreases, the total effect of blocking terrace sites by ethylidyne decreases (Figures 5a and 7). This becomes most apparent for a surface with an average particle size of 2.5 nm as both the CO-IRAS and TPD profiles do not change after exposure to ethylene (Figures 4b and 5a). Also presented in Figure 7 are the site estimates for $C_9^3 + C_{4.5}^8$ and C_9^3 -only terrace sites on the surface of cuboctahedrons of various sizes from V&H¹⁸ along with our counting model labeled “cap $C_9^3 + C_{4.5}^8$ ” from Figure 6. It is easily observed that if the V&H¹⁸ model takes into account both C_9^3 and $C_{4.5}^8$ sites, an overestimate is made from the experimental data. If only C_9^3 sites are assumed, then the V&H model approaches the TDS results for $>3.3\text{ nm}$ NPs but begins to fail while moving

to smaller NPs. The main reason for this deviation is that the V&H model is based on completed cuboctahedron (111) crystal planes. The truncated cubo-octahedron “cap” model, which takes into account both C^3_9 and $C^{4,5}_8$, provides a better fit to the experimental data but deviates for NPs > 4 nm. These results suggest that NPs between 2.5 and 3 nm exhibit a higher concentration of (100) sites and that (111) sites begin to dominate as the particle size increases to 4.2 nm and greater.

Conclusions

Platinum NPs display both terrace and step features in the CO-IRAS and TDS spectra that are comparable to Pt(112) and Pt(335) high index crystal planes but not with Pt(110), Pt(111), or Pt(100) low-index crystal planes. Statistics and experimental results presented here and in the literature demonstrate that Pt NPs begin to deviate from Pt(112) and Pt(335) surfaces as the particle size drops below 4 nm. Despite this behavior, the assignment of terrace and step CO in IRAS and TDS spectra remains valid as NPs become smaller than 4 nm. Separation of terrace and step features in the CO-TDS profiles allows the percentage of terrace sites on Pt NP of varying size to be determined experimentally. As the NP size decreases from 4.2 to 2.5 nm, the terrace feature in the CO-TDS decreases by 50%. The most drastic change in Pt NP terrace sites, C^3_9 and $C^{4,5}_8$, occurs between 2 and 3 nm, and correlates with statistical arguments by V&H.¹⁸

Ethylidyne (derived from ethylene) was employed as a terrace blocking species. Postadsorption of CO was investigated by IRAS on ethylidyne-covered NPs and displayed an intense symmetrical CO stretching feature which is red-shifted relative to clean NPs. CO continues to red-shift $\Delta\nu(\text{CO}) \sim 20 \text{ cm}^{-1}$ as the NP size is increased from 2.6 to 4.2 nm. This single feature, although having approximately the same frequency as CO on a clean NP step site ($\sim 2060 \text{ cm}^{-1}$), cannot be associated with step-only adsorption as indicated by the two CO desorption features in their respective TDS profiles. It can be inferred that both terrace and step sites experience a similar environment on ethylidyne-covered Pt NPs, since only one CO stretching feature but two CO desorption features are observed. Exposure of ethylene to NPs < 2.6 nm has no effect on CO adsorption. This demonstrates ethylidyne formation is inhibited on Pt NPs < 2.6 nm. TDS of CO from ethylidyne-covered NPs was also used to determine the concentration of ethylidyne from a surface with an average particle size $\langle d_p \rangle = 4.2 \text{ nm}$. This was estimated, based on our NP surface density and size distribution estimates from our previous results,²³ to be between ~ 4 and 8 ethylidyne molecules per nanoparticle. This investigation demonstrates a direct correlation between numerical values of site concentrations on Pt nanoparticles from experiment and theoretical models. These results can now be used to correlate active-site concentrations on Pt nanoparticles to selectivity data obtained from elevated pressure reactions in ongoing fundamental investigations being conducted in our laboratory.

Acknowledgment. We gratefully acknowledge support of this work by the Department of Energy, Office of Basic Energy Sciences, Division of Chemical Sciences, Geosciences, and Biosciences (DE-FG02-95ER-14511) and the Robert A. Welch Foundation.

References and Notes

- (1) Xu, X.; Vesecky, S. M.; Goodman, D. W. *Science* **1992**, 258, 788.
- (2) Kalakkad, D.; Anderson, S. L.; Logan, A. D.; Pena, J.; Braunschweig, E. J.; Peden, C. H. F.; Datye, A. K. *J. Phys. Chem.* **1993**, 97, 1437–1444.
- (3) Coulter, K.; Xu, X.; Goodman, D. W. *J. Phys. Chem.* **1994**, 98, 1245–1249.
- (4) Somorjai, G. A.; McCrea, K. R.; Zhu, J. *Top. Catal.* **2002**, 18, 157.
- (5) Silvestre-Albero, J.; Rupprechter, G.; Freund, H. J. *J. Catal.* **2006**, 240, 58–65.
- (6) Kugler, E. L.; Boudart, M. *J. Catal.* **1979**, 59, 201–210.
- (7) Wei, T.; Wang, J.; Goodman, D. W. *J. Phys. Chem. C* **2007**, 111, 8781–8788.
- (8) Stoop, F.; Toolenaar, F. J. C. M.; Ponc, V. *J. Catal.* **1982**, 73, 50–56.
- (9) Xu, J.; Yates, J. T. *Surf. Sci.* **1995**, 327, 193–201.
- (10) Hoffmann, F. M. *Surf. Sci. Rep.* **1983**, 3, 107–192.
- (11) Hollins, P. *Surf. Sci. Rep.* **1992**, 16, 51–94.
- (12) McClellan, M. R.; Gland, J. L.; McFeeley, F. R. *Surf. Sci.* **1981**, 112, 63–77.
- (13) Blackman, G. S.; Kao, C. T.; Bent, B. E.; Mate, C. M.; Van Hove, M. A.; Somorjai, G. A. *Surf. Sci.* **1988**, 207, 66.
- (14) Beebe, T. P.; Yates, J. T. *Surf. Sci.* **1986**, 173, L606–L612.
- (15) Gross, E.; Asscher, M.; Lundwall, M.; Goodman, D. W. *J. Phys. Chem. C* **2007**, 111, 16197–16201.
- (16) Vattuone, L.; Savio, L.; Rocca, M. *Surf. Sci. Rep.* **2008**, 63, 101–168.
- (17) Valden, M.; Lai, X.; Goodman, D. W. *Science* **1998**, 281, 1647.
- (18) Van Hardeveld, R.; Hartog, F. *Surf. Sci.* **1969**, 15, 189–230.
- (19) Goodman, D. W. *J. Phys. Chem.* **1996**, 100, 13090–13102.
- (20) St. Clair, T. P.; Goodman, D. W. *Top. Catal.* **2000**, 13, 5–19.
- (21) Haq, S.; Raval, R. *Phys. Chem. Chem. Phys.* **2007**, 9, 3641–3647.
- (22) McClure, S. M.; Lundwall, M.; Yang, F.; Zhou, Z.; Goodman, D. W. *J. Phys.: Condens. Matter* **2009**, 21, 474223.
- (23) McClure, S. M.; Lundwall, M.; Zhou, Z.; Yang, F.; Goodman, D. W. *Catal. Lett.* **2009**, 133, 298–306.
- (24) McClure, S. M.; Lundwall, M.; Yang, F.; Zhou, Z.; Goodman, D. W. *J. Phys. Chem. C* **2009**, 113, 9688–9697.
- (25) Freund, H. J. *Top. Catal.* **2008**, 48, 137–144.
- (26) Henry, C. R. *Surf. Sci. Rep.* **1998**, 31, 231–325.
- (27) Altman, E. I.; Gorte, R. J. *Surf. Sci.* **1986**, 172, 71–80.
- (28) Hensley, D. A.; Kesmodel, L. L. *J. Phys. Chem.* **1991**, 95, 1363–1373.
- (29) Morgan, A. E.; Somorjai, G. A. *Surf. Sci.* **1968**, 12, 405–425.
- (30) Morgan, A. E.; Somorjai, G. A. *J. Chem. Phys.* **1969**, 51, 3309.
- (31) Fair, J.; Madix, R. J. *J. Chem. Phys.* **1980**, 73, 3480.
- (32) Malik, I. J.; Brubaker, M. E.; Mohsin, S. B.; Trenary, M. *J. Chem. Phys.* **1987**, 87, 5554.
- (33) Starke, U.; Barbieri, A.; Materer, N.; Van Hove, M. A.; Somorjai, G. A. *Surf. Sci.* **1993**, 286, 1–14.
- (34) Cremer, P. S.; Su, X.; Shen, Y. R.; Somorjai, G. A. *J. Am. Chem. Soc.* **1996**, 118, 2942–2949.
- (35) Chen, P.; Kung, K. Y.; Shen, Y. R.; Somorjai, G. A. *Surf. Sci.* **2001**, 494, 289–297.
- (36) Stacchiola, D.; Kaltchev, M.; Wu, G.; Tysse, W. T. *Surf. Sci.* **2000**, 470, L32–L38.
- (37) Rioux, R. M.; Hoefelmeyer, J. D.; Grass, M.; Song, H.; Nies, K.; Yang, P.; Somorjai, G. A. *Langmuir* **2008**, 24, 198–207.
- (38) Frank, M.; Baumer, M.; Kuhnemuth, R.; Freund, H. J. *J. Vac. Sci. Technol. A* **2001**, 19, 1497.
- (39) Ainsworth, M. K.; McCoustra, M. R. S.; Chesters, M. A.; Sheppard, N.; De La Cruz, C. *Surf. Sci.* **1999**, 437, 9–17.
- (40) Besocke, K.; Krah-Urb, B.; Wagner, H. *Surf. Sci.* **1977**, 68, 39–46.
- (41) Hammer, B.; Nielsen, O. H.; Norskov, J. K. *Catal. Lett.* **1997**, 46, 31–35.
- (42) Szanyi, J.; Goodman, D. W. *Rev. Sci. Instrum.* **1993**, 64, 2350.
- (43) Chen, M. S.; Santra, A. K.; Goodman, D. W. *Phys. Rev. B* **2004**, 69, 155404-1–155404-7.
- (44) Xu, X.; Goodman, D. W. *Appl. Phys. Lett.* **1992**, 61, 774.
- (45) Wang, H.; Tobin, R. G.; Lambert, D. K. *J. Chem. Phys.* **1994**, 101, 4277.
- (46) Gracia, F. J.; Bollmann, L.; Wolf, E. E.; Miller, J. T.; Kropf, A. J. *J. Catal.* **2003**, 220, 382–391.
- (47) Hayden, B. E.; Kretzschmar, K.; Bradshaw, A. M.; Greenler, R. G. *Surf. Sci.* **1985**, 149, 394–406.
- (48) Luo, J. S.; Tobin, R. G.; Lambert, D. K.; Fisher, G. B.; DiMaggio, C. L. *J. Chem. Phys.* **1993**, 99, 1347.
- (49) Brandt, R. K.; Greenler, R. G. *Chem. Phys. Lett.* **1994**, 221, 219–223.
- (50) Wang, H.; Tobin, R. G.; Lambert, D. K.; Fisher, G. B.; DiMaggio, C. L. *J. Phys. Chem.* **1995**, 103, 2711.
- (51) Creighan, S. C.; Mukerji, R. J.; Bolina, A. S.; Lewis, D. W.; Brown, W. A. *Catal. Lett.* **2003**, 88, 39.
- (52) Mukerji, R. J.; Bolina, A. S.; Bown, W. A. *Surf. Sci.* **2003**, 527, 198–208.
- (53) McCabe, R. W.; Schmidt, L. D. *Surf. Sci.* **1977**, 66, 101–124.

- (54) Ramachandran, A. S.; Anderson, S. L.; Dayte, A. K. *Ultramicroscopy* **1993**, *51*, 282–297.
- (55) Lee, W. H.; Vanloon, K. R.; Petrova, V.; Woodhouse, J. B.; Loxton, C. M.; Masel, R. I. *J. Catal.* **1990**, *126*, 658–671.
- (56) Shi, A.-C.; Masel, R. I. *J. Catal.* **1989**, *120*, 421–431.
- (57) Wang, T.; Lee, C.; Schmidt, L. D. *Surf. Sci.* **1985**, *163*, 181–197.
- (58) Minors, J. H.; Gardner, P.; Woodruff, D. P. *Surf. Sci.* **2003**, *547*, 355–373.
- (59) Van Hove, M. A.; Somorjai, G. A. *Surf. Sci.* **1980**, *92*, 489–518.
- (60) Savio, L.; Vattuone, L.; Rocca, M. *Phys. Rev. Lett.* **2001**, *87* (24), 276101.
- (61) Kose, R.; King, D. A. *Chem. Phys. Lett.* **1999**, *313*, 1–6.
- (62) Zafiris, G. S.; Gorte, R. J. *J. Catal.* **1993**, *140*, 418–423.
- (63) Greenler, R. G.; Burch, K. D.; Kretzschmar, K.; Klauser, R.; Bradshaw, A. M.; Hayden, B. E. *Surf. Sci.* **1985**, *152/153*, 338–345.
- (64) Barth, R.; Pitchai, R.; Anderson, R. L.; Verykios, X. E. *J. Catal.* **1989**, *116*, 61–70.
- (65) De La Cruz, C.; Sheppard, N. *Spectrochim. Acta* **1994**, *50A*, 271–285.
- (66) Fox, S. G.; Browne, V. M.; Hollins, P. J. *Electron Spectrosc. Relat. Phenom.* **1990**, *54/55*, 749–758.
- (67) Brandt, R. K.; Sorbello, R. S.; Greenler, R. G. *Surf. Sci.* **1992**, *271*, 605–615.
- (68) Kappers, M. J.; Van Der Mass, J. H. *Catal. Lett.* **1991**, *10*, 365–374.
- (69) Brandt, R. K.; Hughes, M. R.; Bourget, L. P.; Truszkowska, K.; Greenler, R. G. *Surf. Sci.* **1993**, *286*, 15–25.
- (70) Eischens, R. P.; Francis, S. A.; Pliskin, W. A. *J. Phys. Chem.* **1956**, *60*, 194.
- (71) Hammaker, R. M.; Francis, S. A.; Eischens, R. P. *Spectrochim. Acta* **1965**, *21*, 1295–1309.
- (72) Martin, R.; Gardner, P.; Bradshaw, A. M. *Surf. Sci.* **1995**, *342*, 69–84.
- (73) Wang, P.; Slichter, C. P.; Sinfelt, J. H. *J. Phys. Chem.* **1985**, *89*, 3606–3609.
- (74) Beebe, T. P.; Yates, J. T. *J. Phys. Chem.* **1987**, *91*, 254–257.
- (75) Chesters, M. A.; De La Cruz, C.; Gardner, P.; McCash, E. M.; Prentice, J. D.; Sheppard, N. *J. Electron Spectrosc. Relat. Phenom.* **1990**, *54/55*, 739–748.
- (76) Paul, D. K.; Beebe, T. P.; Uram, K. J.; Yates, J. T. *J. Am. Chem. Soc.* **1992**, *114*, 1949–1954.
- (77) Blyholder, G. *J. Phys. Chem.* **1964**, *68*, 2772.
- (78) Gumhalter, B.; Hermann, K.; Wandelt, K. *Vacuum* **1990**, *41*, 1–3.

JP9119292